

SEARCH FOR RESONANT DOUBLE HIGGS PRODUCTION WITH BBZZ
DECAYS IN THE $b\bar{b}\ell\ell\nu\bar{\nu}$ FINAL STATE IN pp COLLISIONS AT $\sqrt{s} = 13$ TeV

by

Rami Kamalieddin

A DISSERTATION

Presented to the Faculty of
The Graduate College at the University of Nebraska
In Partial Fulfilment of Requirements
For the Degree of Doctor of Philosophy

Major: Physics and Astronomy

Under the Supervision of Professor Ilya Kravchenko

Lincoln, Nebraska

May, 2019

SEARCH FOR RESONANT DOUBLE HIGGS PRODUCTION WITH BBZZ
DECAYS IN THE $b\bar{b}\ell\ell\nu\bar{\nu}$ FINAL STATE IN pp COLLISIONS AT $\sqrt{s} = 13$ TeV

Rami Kamalieddin, Ph.D.

University of Nebraska, 2019

Advisers: Ilya Kravchenko

Since the discovery of the Higgs boson in 2012 by the A Toroidal LHC ApparatuS (ATLAS) and The Compact Muon Solenoid (CMS), most of the quantum mechanical properties that describe the long-awaited Higgs boson have been measured. Due to an impeccable work of the LHC, dozens of fb^{-1} of data have been delivered to both experiments. Finally, it became possible for analyses that have a very low cross section to observe rare decay modes of the Higgs boson, as was done successfully recently in ttH and VHbb channels. The only untouched territory is a double Higgs boson production. Data will not help us much either at the HL-LHC, the process will remain unseen even in the most optimistic scenarios, so one has to rely solely on new reconstruction methods as well as new analysis techniques. This thesis is addressing both goals. I have been blessed by an opportunity to work in the CMS electron identification group, where we have developed new electron identification algorithms. The majority of this thesis, however, will be devoted to the second goal of HL-LHC. We establish the techniques for the first ever analysis at the LHC that searches for the double Higgs production mediated by a heavy narrow-width resonance in the $b\bar{b}ZZ$ channel: $X \rightarrow HH \rightarrow b\bar{b}ZZ^* \rightarrow b\bar{b}\ell\ell\nu\bar{\nu}$. The analysis searches for a resonant production of a Higgs boson pair in the range of masses of the resonant parent particle from 250 to 1000 GeV. Both spin scenarios of the resonance are considered: spin 0 (later called "graviton") and spin 2 (later called "radion"). In the absence of the

evidence of the resonant double Higgs boson production from the previous searches, we set upper confidence limits. When combined with other search channels, this analysis will contribute to the discovery of the double Higgs production and we would be able to finally probe the Higgs boson potential using its self-coupling.

“... a place for a smart quote!”

Lenin, 1922.

ACKNOWLEDGMENTS

This will be a longgggg list!

Table of Contents

List of Figures	viii
List of Tables	x
1 LHC and the CMS experiment	1
1.1 Introduction	1
1.2 The LHC	4
1.2.1 The Magnets	4
1.2.2 Radio Frequency System	6
1.2.3 Vacuum System	7
1.2.4 Powering	8
1.2.5 Cryogenic system	9
1.2.6 Beam dumping system	11
1.2.7 Beam injection system	12
1.2.8 LHC injection chain	12
1.3 The CMS experiment	14
1.3.1 CMS coordinate system	17
1.3.2 Tracking system	18
1.3.3 Silicon strip tracker	21

1.3.4	Electromagnetic calorimeter	23
1.3.5	Hadronic calorimeter	25
1.3.6	Superconducting solenoid magnet	26
1.3.7	Muon system	27
1.3.8	CMS trigger system	28
1.3.9	CMS computing	30
Bibliography		33
References		34

List of Figures

1.1	Schematic layout of the LHC.	3
1.2	The cross section of the LHC dipole	5
1.3	Cables of the dipole magnet	6
1.4	RF cavities module.	6
1.5	Beam screen.	8
1.6	13 kA high-temperature superconducting current lead.	9
1.7	Cross section of the LHC tunnel	10
1.8	LHC cryogenic states and the temperature scale.	11
1.9	LHC injection complex.	12
1.10	Layout of the CMS detector	14
1.11	CMS detector transverse slice	16
1.12	CMS detector coordinate system	17
1.13	CMS tracking system schematic view.	19
1.14	CMS pixel detector	20
1.15	SST Schematic view.	22
1.16	CMS ECAL schematic view	24
1.17	CMS HCAL schematic view	25
1.18	CMS solenoid magnet	26

1.19 CMS Muon system schematic view	27
1.20 CMS Level-1 trigger architecture	29
1.21 WLCG structure	31
1.22 Data flow from CMS detector through hardware Tiers	33

List of Tables

CHAPTER 1

LHC and the CMS experiment

1.1 Introduction

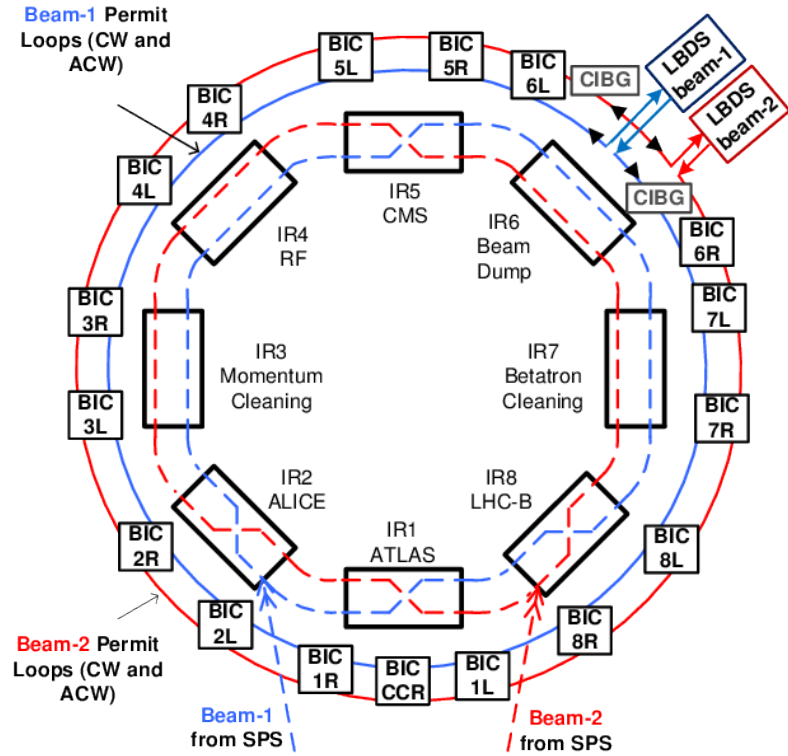
Large Hadron Collider (LHC) (see Fig. 1.1) is the most powerful particle accelerator that has ever been built. It is located at the border of the France and Switzerland, reutilising the tunnel used previously by the Large Electron Positron collider. The whole LHC story begins in 1977, when CERN director general Sir John Adams suggested that LEP tunnel can be reused to accommodate the future hadron collider of more than 3 TeV energies ???. At the 1984 ECFA-CERN workshop on a "Large Hadron Collider in the LEP Tunnel" ??, the plans for LHC were stated, where the primary ones were the BEH mechanism, Higgs boson, and the origin of masses of W and Z bosons". The parameters of the LHC were very ambitious, the centre-of-mass energy of 10 to 20 TeV, and a target luminosity of $10^{33-34} \frac{1}{cm^2 s}$. Luminosity is the coefficient which refers the cross section of the event under study to the number of events that will be generated in the LHC collision: $N_{events} = L\sigma_{event}$. Luminosity is the parameter control by the machine and for Gaussian beams ?? can be written as:

$$L = \frac{N_b^2 n_b f_{rev} \gamma_r}{4\pi \varepsilon_n \beta^*} F$$

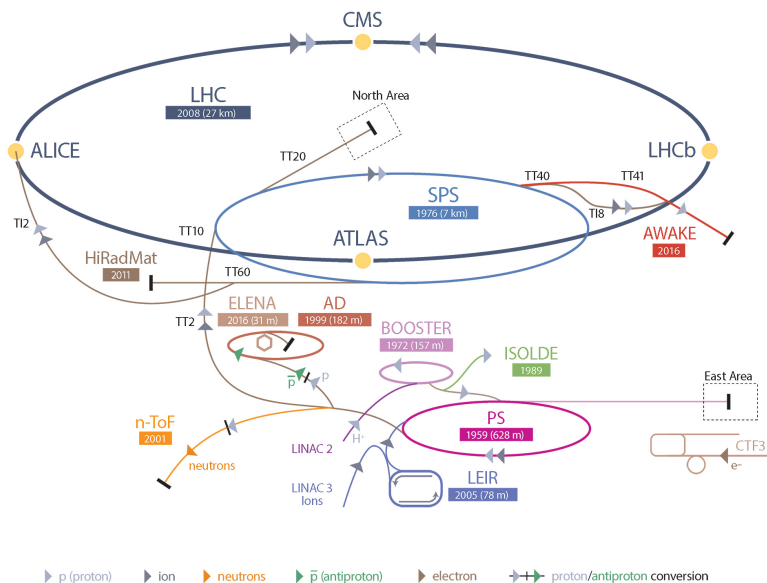
where N_b is the number of particle in the colliding bunch, n_b is the number of colliding bunches in the beam, f_{rev} is the revolution frequency, γ_r is the relativistic

factor, ε_n is the normalised transverse beam emittance, β^* is the beta function at the collision point, and F is the factor related to the crossing angle at the interaction point (IP). The luminosity is not constant and decays with time due to the degradation of the initial circulating beams. Decay time is approximately 45 h with 29 h to reach $1/e$ level. Adding contribution from the intrabeam scattering, scattering on the residual gas, etc, the final luminosity lifetime is about 15 h. Another useful variation of the luminosity parameter is an integrated luminosity. Integrating over the yield of a single run we get:

$L_{int} = L_0 \tau_L \left[1 - e^{-\frac{T_{run}}{\tau_L}} \right]$, where L_0 is the initial luminosity, T_L is the total length of the run, and τ_L is the luminosity lifetime. The optimum runtime thus is either 5.5 or 12 hours, which potentially leads to $80 - 120/fb$ of data with barn b denoting a unit area of $10^{28} m^2$.



CERN's Accelerator Complex

**Figure 1.1:** Schematic layout of the LHC.

1.2 The LHC

The first LHC budget plan was approved in 1996 and the final cost sum was completed in 2008. 4 years later the Higgs discovery happened, in 2012, quite fast for such a huge project! Now we will talk about the most important parts of the LHC complex one-by-one. Let us start with magnets.

1.2.1 The Magnets

To keep the beam of protons on a circular orbit LHC needs strong magnets. The proven technology existed since Tevatron and relied on $NbTi$ superconductors. 1232 dipoles at $8\text{ }T$, which are cooled to the below $2\text{ }K$ temperature using superfluid Helium, bend the beam 1.2. The dipole cold mass is in the so-called Helium bath and is cooled down to $1.9\text{ }K$. Each of the $16.5\text{ }m$ (with ancillaries) long and $570\text{ }mm$ in diameter dipoles is slightly curved by $5.1\text{ }mrad$ to help a chain of dipoles complete 360 degrees. The dipole is located inside of the dipole cryostat, which is a long cylindrical tube $914\text{ }mm$ in diameter made of low-carbon steel. During the standard operation time the vessel contains the vacuum.

LHC DIPOLE : STANDARD CROSS SECTION

CERN AC/DI/MM - HE107 - 30 04 1999

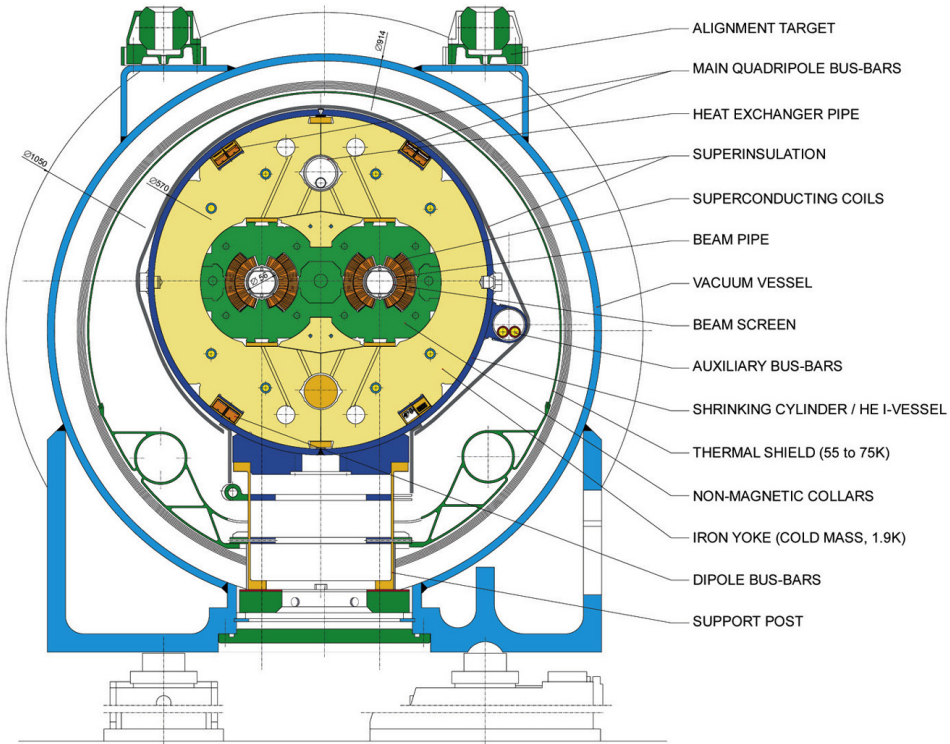


Figure 1.2: The cross section of the LHC dipole.

The material and the properties of the cables for the dipoles had to be carefully chosen. Each dipole coil is 56 mm in diameter and is made of cables of two types. The cable in the inner layer contains 28 strands 1.065 mm each. The outer layer contains 36 strands 0.825 mm each 1.3.

To correct the orbit, higher order correctors are used with about 3800 single aperture and 1000 twin aperture magnets evenly spaced around the circular trajectory.

Another important task that is performed with the use of magnets is the beam insertion, which is done at eight specific insertion locations. LHC also uses *NbTi* magnets to accomplish this work.

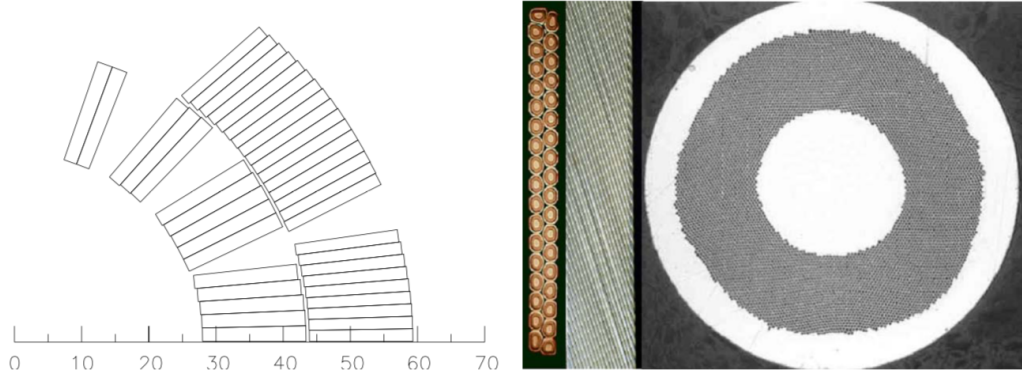


Figure 1.3: Cables of the dipole magnet. Left: cross section view. Right: Strand and cables

1.2.2 Radio Frequency System

The beam that comes from injectors will be placed, accelerated and kept on the orbit with the help of Radio Frequency (RF) cavities. The same system will be used to correct for injection errors in the beam direction. RF will be operating at the 400 *MHz*, which is 10 times more than the revolution frequency of 40 *MHz*.

Four RF cavities grouped together into one cryomodule constitute an important accelerating module. If something happens to this module, it can be easily replaced in short period of time.

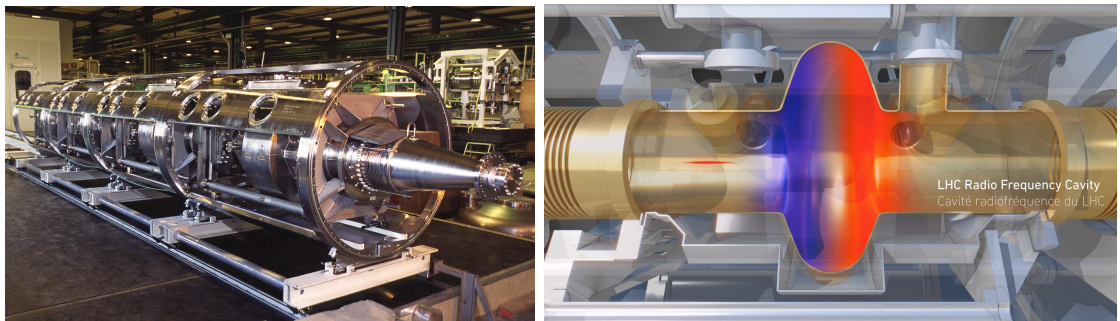


Figure 1.4: LHC RF cavities. Right: a single RF cavity schematic drawing. The colour field is used to highlight the fact of two field of the different polarity. Left: a cryomodule with four RF cavities.

1.2.3 Vacuum System

Three types of vacuum systems are necessary for the LHC proper operation. The vacuum system for the cryomagnets, the insulation vacuum for helium distribution, and, of course, the vacuum for the beam (VBS). As a convention, taking into account ionisation cross sections for gasses of the interests, cryogenic temperatures are expressed as corresponding gas densities normalised to the hydrogen. VBS, to ensure the 100 hours long run time, requires the equivalent hydrogen densities (EHD) to be below $10^{15} H_2 \frac{1}{m^3}$. To minimise the backgrounds from the experiments, the EHD at the interaction points should be $10^{13} H_2 \frac{1}{m^3}$. Those parts of the beam system, which operate under room temperatures, are under the pressure of 10^{-10} to 10^{-11} mbar. All the vacuum section are subdivided into smaller modules to allow easy repair and fine tuning. VBS, as the most demanding in terms of the vacuum quality, have to be properly designed and must address a number of challenges, such as synchrotron radiation that significantly affects vacuum chambers in the arcs around the tunnel, as well as an electron cloud effect which exists along the length of the whole circle of the LHC. After the beam is inserted and is stabilised, the final adjustment of the VBS is needed to guarantee the perfect performance.

To finish the discussion of the VBS, let us discuss which heat sources have the main effect on the vacuum of the beam that must exist at the 1.9 K.

- Synchrotron radiation ($0.2 W/m$ per beam)
- Energy loss by nuclear scattering ($30 mW/m$ per beam)
- Image currents ($0.2 W/m$ per beam)
- Electron cloud related effects (vary)

To obstruct the heat sources mentioned above, specific beam screens are developed. Screens have elliptical shape, so-called racetrack shape, which gives extra space for cooling while optimises the aperture. Finally, the lifetime of the vacuum is mostly determined by the interactions of the vacuum gas nuclei with the protons of the beam. Values of the cross sections of such processes are given in ??.

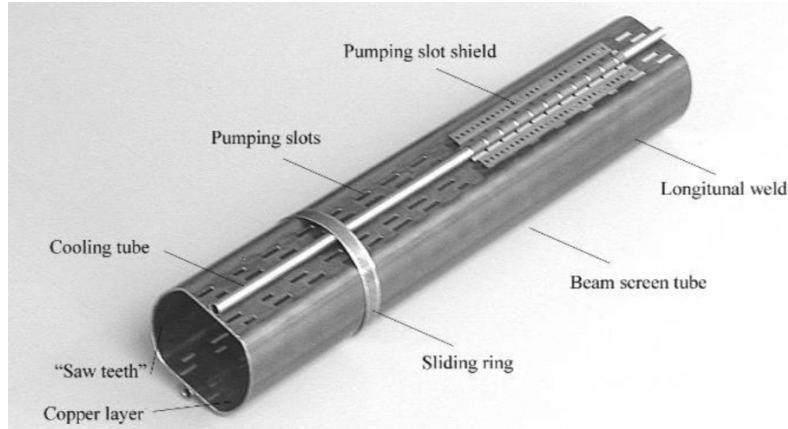


Figure 1.5: Beam screen.

1.2.4 Powering

To power the LHC, 1612 electrical circuits of 131 types are used. The magnets are powered in eight symmetrical sections. Some sections rely on all 131 types of circuits, while others may use only specific ones. To power the main quadrupoles which focus the beam, the power converters are located in the underground area. A total of 3286 current leads is needed to connect all the circuits and power cables. 1070 of the leads operate between 600 A and 13 kA. The other leads work in the range 60 to 120 A.



Figure 1.6: 13 kA high-temperature superconducting current lead.

1.2.5 Cryogenic system

The cryogenic system must supply the LHC cold mass of 37 Mkg within 15 days with the necessary temperature settings and work with the temperatures different by 75 K. The system must also be able to deal with the fast pressure raises and flow surges, and should be able to recover in a short period of time from such perturbations not to affect the run of the whole LHC. Another important point during the cryogenic design that had to be addressed is the fact that the LHC tunnel is inclined in the

horizontal plane by 1.41° . This equals to 120 m difference in the vertical location of two diametrically opposite points of the tunnel with respect to the surface level and results in the additional hydrostatic pressure that can affect the flow of the cryogen. To avoid any instability of the LHC work like this, the gas is transported in the super-heated-vapour state.

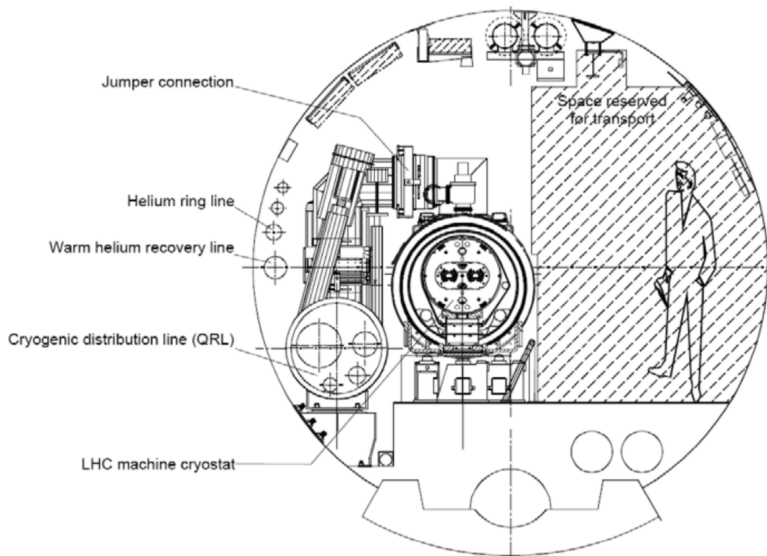


Figure 1.7: Cross section of the LHC tunnel

Since the cost of the production of 1.8 K temperature is high, several temperature levels are employed:

- 50 to 75 K to the thermal shielding that protects the cold masses
- 4.6 to 20 K for lower temperature interception and to cool the beam screens
- 1.9 K for quasi-isothermal helium in the superfluid state to cool the magnet cold mass
- 4 K for the transportation system that directs the 1.8 K helium from the exchanger to the 1.8 K refrigerator

- 4.5 K for RF cavities and lower sections of the high-temperature superconducting current leads
- 20 to 300 K for upper sections of the high-temperature superconducting current leads

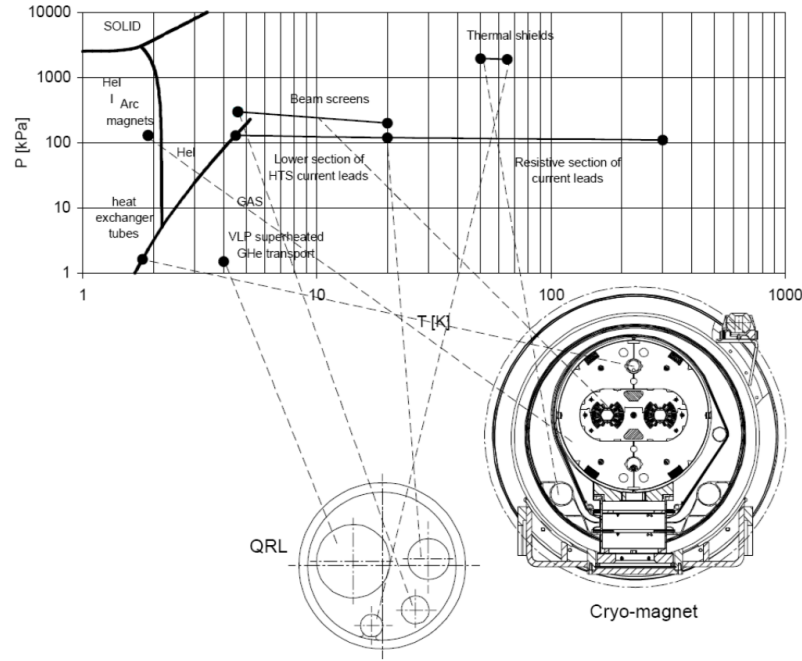


Figure 1.8: LHC cryogenic states and the temperature scale.

1.2.6 Beam dumping system

The LHC beam carries a lot of power and a well-designed and reliable beam extraction and dumping system is needed. Point 6 at LHC contains such system, which is able to fast-extract the beam in a loss-free way. The system for each ring comprises:

- 15 kicker magnets for extraction
- 15 steel septum magnets around the Point 6 interaction point
- 10 modules of the dilution kicker magnets

- the beam dump proper with the associated steel and concrete for shielding
- dedicated dilution devices

1.2.7 Beam injection system

The injection at LHC is done at two points and for two beams separately: at Point 2 and Point 8. The beam comes to the insertion point from outside and below the machine level. A series of magnets and kicker then deflects the beam horizontally and vertically to place the beam on the LHC orbit. To protect against the problematic injections and malfunctioning of the kickers, a series of the collimators correct the incoming beam.

The LHC injection complex

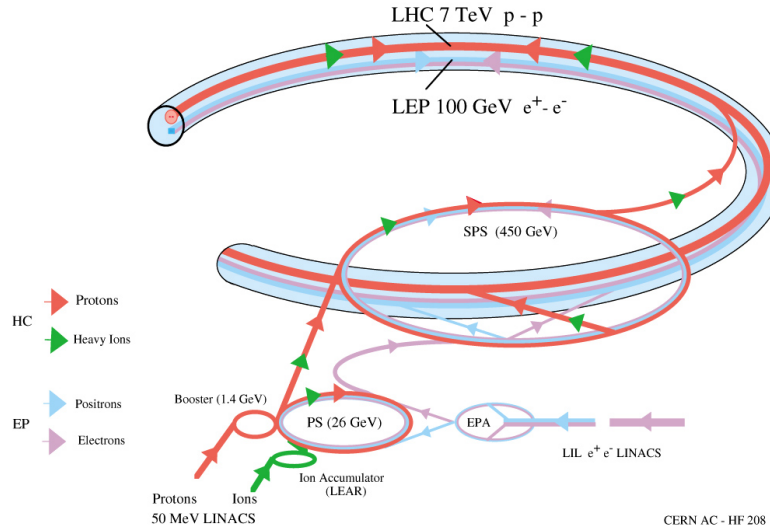


Figure 1.9: LHC injection complex.

1.2.8 LHC injection chain

To place the beam at the final LHC orbit, the protons from the hydrogen bottle extracted from the hydrogen gas reservoir have to travel a long pass during which

they are put into bunches and accelerated to the nominal collision speed.

The acceleration complex consists of: LINAC, Booster, Proton Synchrotron, Super Proton Synchrotron, and finally, the LHC main ring (see Fig. ??).

The whole LHC complex has to satisfy requirements of the final ring, such as:

- the beam emittance has to be compatible with the small aperture of the LHC superconducting magnets
- the effect of the synchrotron radiation has to be taken into account when calculating the required cryogen needs for the intensity of the incoming beam
- the beam-beam interactions that enhance the betatron oscillations
- in the injector the space-charge limits have to be taken into account

1.3 The CMS experiment

CMS is a general-purpose detector designed to conduct research in a wide range of physics from the standard model to new physics like extra dimensions and dark matter. Located at Point 5 in the LHC layout as shown in Figure ??, CMS is composed of several detection systems distributed in a cylindrical structure; in total, CMS weights about 12500 tons in a very compact 21.6 m long and 14.6 m diameter cylinder. It was built in 15 separate sections at the ground level and lowered to the cavern individually to be assembled. A complete and detailed description of the CMS detector and its components is given in Reference [?] on which this section is based. Figure 1.10 shows the layout of the CMS detector. The detection system is composed of (from the innermost to the outermost)

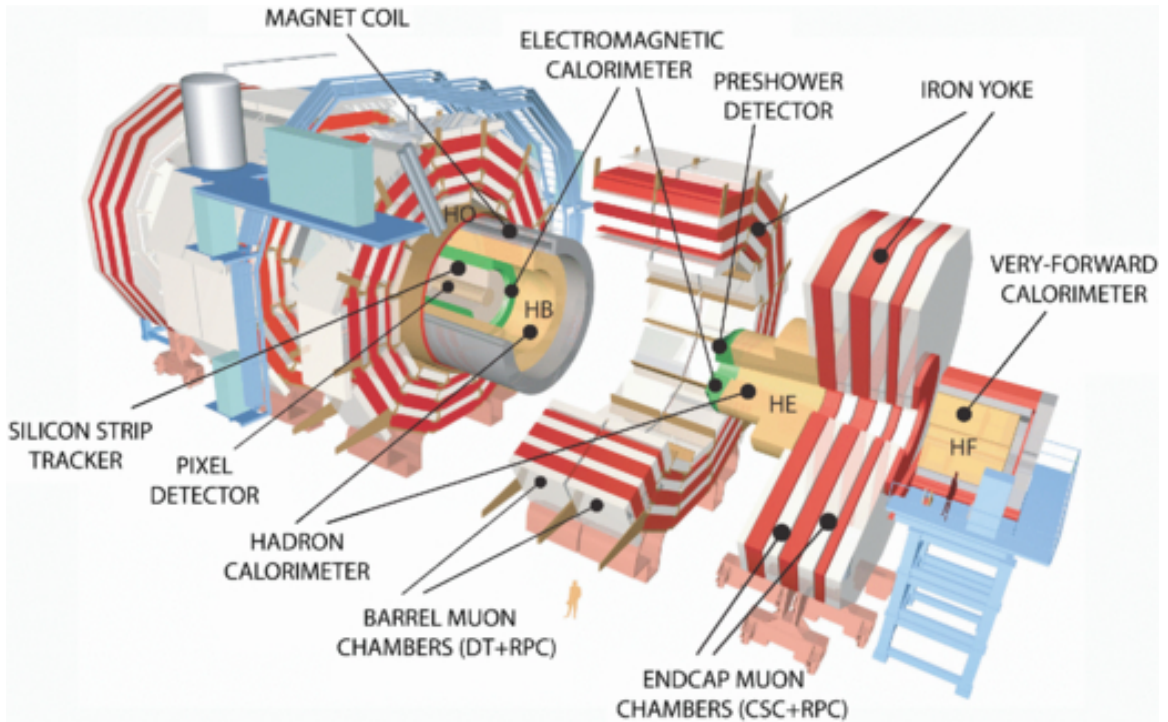


Figure 1.10: Layout of the CMS detector. The several subdetectors are indicated. The central region of the detector is referred as the barrel section while the endcaps are referred as the forward sections. [?].

- Pixel detector.
- Silicon strip tracker.
- Preshower detector.
- Electromagnetic calorimeter.
- Hadronic calorimeter.
- Muon chambers (barrel and endcap)

The central region of the detector is commonly referred as the barrel section while the endcaps are referred as the forward sections of the detector; thus, each subdetector is composed of a barrel section and a forward section.

When a pp collision happens inside the CMS detector, many different particles are produced, but only some of them live long enough to be detected; they are electrons, photons, pions, kaons, protons, neutrons and muons; neutrinos are not detected by the CMS detector. Thus, the CMS detector was designed to detect those particles and measure their properties. Figure 1.11 shows a transverse slice of the CMS detector. The silicon tracker (pixel detector + strip tracker) is capable to register the track of the charged particles traversing it, while calorimeters (electromagnetic and hadronic) measure the energy of the particles that are absorbed by their materials. Considering the detectable particles, mentioned above, emerging from the IP, a basic description of the detection process is as follows.

A muon emerging from the IP, will create a track on the silicon tracker and on the muon chambers. The design of the CMS detector is driven by the requirements on the identification, momentum resolution and unambiguous charge determination of the muons; therefore, a large bending power is provided by the solenoid magnet

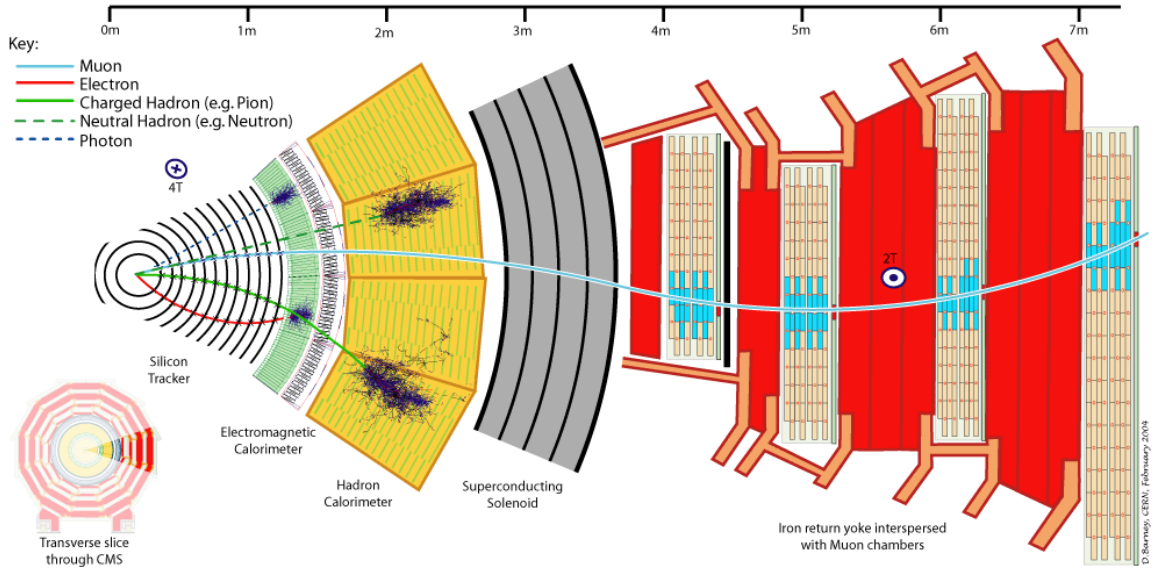


Figure 1.11: CMS detector transverse slice [?].

made of superconducting cable capable of generating a 3.8 T magnetic field. The muon track is bent twice since the magnetic field inside the solenoid is directed along the z -direction but outside its direction is reversed. Muons interact very weakly with the calorimeters, therefore, it is not absorbed but escape away from the detector.

An electron emerging from the IP will create a track along the tracker which will be bent due to the presence of the magnetic field, later, it will be absorbed in the electromagnetic calorimeter where its energy is measured.

A photon will not leave a track because it is neutral, but it will be absorbed in the electromagnetic calorimeter.

A neutral hadron, like the neutron, will not leave a track either but it will lose a small amount of its energy during its passage through the electromagnetic calorimeter and then it will be absorbed in the hadron calorimeter depositing the rest of its energy.

A charged hadron, like the proton or π^\pm , will leave a curved track on the silicon tracker, some of its energy in the electromagnetic calorimeter and finally will be absorbed in the hadronic calorimeter.

A more detailed description of each detection system will be presented in the following sections.

1.3.1 CMS coordinate system

The coordinate system used by CMS is centered on the geometrical center of the detector which is the nominal IP as shown in Figure 1.12¹. The z -axis is parallel to the beam direction, while the Y -axis pointing vertically upward, and the X -axis pointing radially inward toward the center of the LHC.

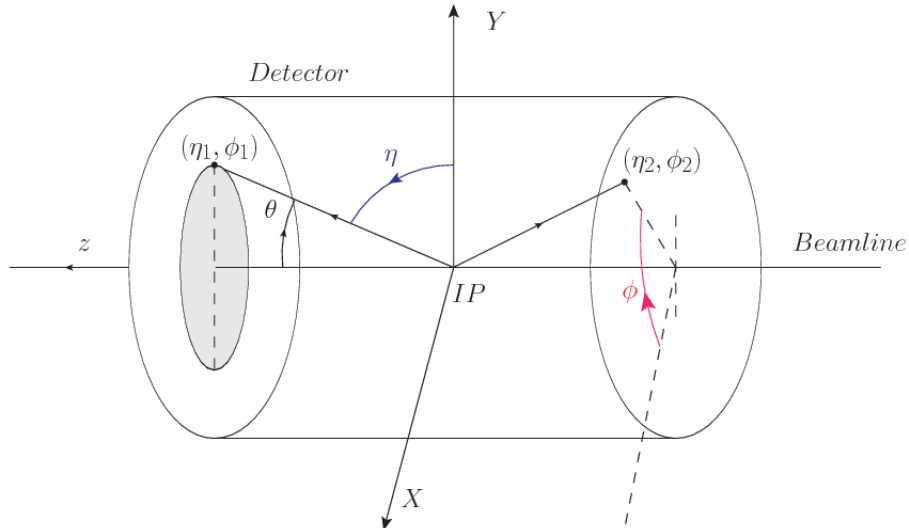


Figure 1.12: CMS detector coordinate system.

In addition to the common cartesian and cylindrical coordinate systems, two coordinates are of particular utility in particle physics: rapidity (y) and pseudorapidity (η), defined in connection to the polar angle θ , energy and longitudinal momentum component (momentum along the z -axis) according to

$$y = \frac{1}{2} \ln \frac{E + p_z}{E - p_z} \quad \eta = -\ln \left(\tan \frac{\theta}{2} \right) \quad (1.1)$$

¹ Not all the pp interaction occur at the nominal IP because of the bunch lenght, therefore, each pp collision has it own IP location

Rapidity is related to the angle between the XY -plane and the direction in which the products of a collision are emitted; it has the nice property that the difference between the rapidities of two particles is invariant with respect to Lorentz boosts along the z -axis, hence, data analysis becomes more simple when based on rapidity; however, it is not simple to measure the rapidity of highly relativistic particles, as those produced after pp collisions. Under the highly relativistic motion approximation, y can be rewritten in terms of the polar angle, concluding that rapidity is approximately equal to the pseudorapidity defined above, i.e., $y \approx \eta$. Note that η is easier to measure than y given the direct relationship between the former and the polar angle.

The angular distance between two objects in the detector (ΔR) is commonly used to judge the isolation of those object; it is defined in terms of their coordinates (η_1, ϕ_1) , (η_2, ϕ_2) as

$$\Delta R = \sqrt{(\Delta\eta)^2 - (\Delta\phi)^2} \quad (1.2)$$

1.3.2 Tracking system

The CMS tracking system is designed to provide a precise measurement of the trajectories (*track*) followed by the charged particles created after the pp collisions; also, the precise reconstruction of the primary and secondary origins of the tracks (*vertices*) is expected in an environment where, each 25 ns, the bunch crossing produces about 20 inelastic collisions and about 1000 particles.

Physics requirements guiding the tracking system performance include the precise characterization of events involving gauge bosons, W and Z, and their leptonic decays for which an efficient isolated lepton and photon reconstruction is of capital importance, given that isolation is required to suppress background events to a level

that allows observations of interesting processes like Higgs boson decays or beyond SM events.

The ability to identify and reconstruct b -jets and B-hadrons within these jets is also a fundamental requirement, achieved through the ability to reconstruct accurately displaced vertices, given that b -jets are part of the signature of top quark physics, like the one treated in this thesis.

An schematic view of the CMS tracking system is shown in Figure 1.13

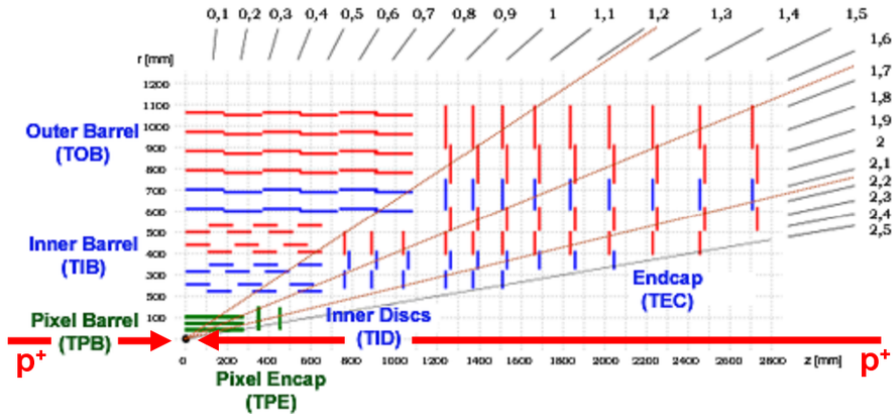


Figure 1.13: CMS tracking system schematic view [?].

In order to satisfy these performance requirements, the tracking system uses two different detector subsystems arranged in concentric cylindrical volumes, the pixel detector and the silicon strip tracker; the pixel detector is located in the high particle density region ($r < 20$ cm) while the silicon strip tracker is located in the medium and lower particle density regions $20 \text{ cm} < r < 116 \text{ cm}$.

Pixel detector

The pixel detector was replaced during the 2016-2017 extended year-end technical stop, due to the increasingly challenging operating conditions like the higher particle flux and more radiation harsh environment, among others. The new one is responding

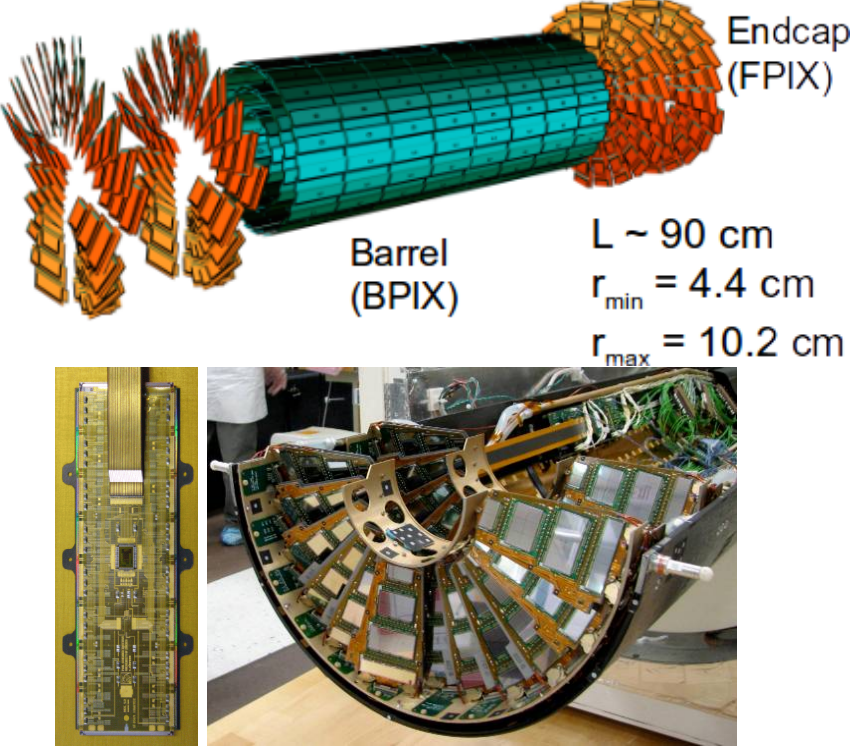


Figure 1.14: CMS pixel detector. Top: schematic view; Bottom: pictures of a barrel(BPIX) module(left) and forward modules(right) [?].

as expected, reinforcing its crucial role in the successful way to fulfill the new LHC physics objectives after the discovery of the Higgs boson. Since the data sets used in this thesis were produced using the previous version of the pixel detector, it will be the subject of the description in this section. The last chapter of this thesis is dedicated to describe my contribution to the *Forward Pixel Phase 1 upgrade*.

The pixel detector was composed of 1440 silicon pixel detector modules organized in three-barrel layers in the central region (BPix) and two disks in the forward region (FPix) as shown in the top side of Figure 1.14; it was designed to record efficiently and with high precision, up to $20 \mu\text{m}$ in the XY -plane and $20 \mu\text{m}$ in the z -direction, the first three space-points (*hits*) nearest to the IP region in the range $|\eta| \leq 2.5$. The first barrel layer was located at a radius of 44 mm from the beamline, while the third

layer was located at a radius of 102 mm, closer to the strip tracker inner barrel layer (see Section 1.3.3) in order to reduce the rate of fake tracks. The high granularity of the detector is represented in its about 66 Mpixels, each of size $100 \times 150 \mu\text{m}^2$. The transverse momentum resolution of tracks can be measured with a resolution of 1-2% for muons of $p_T = 100$ GeV.

A charged particle passing through the pixel sensors produce ionization in them, giving energy for electrons to be removed from the silicon atoms, hence, creating electron-hole pairs. The collection of charges in the pixels generates an electrical signal that is read out by an electronic readout chip (ROC); each pixel has its own electronics which amplifies the signal. Combining the signal from the pixels activated by a traversing particle in the several layers of the detector allows one to reconstruct the particle's trajectory in 3D.

Commonly, the charge produced by traversing of a particle is collected by and shared among several pixels; by interpolating between pixels, the spatial resolution is improved. In the barrel section the charge sharing in the $r\phi$ -plane is due to the Lorentz effect. In the forward pixels the charge sharing is enhanced by arranging the blades in the turbine-like layout as shown in Figure 1.14 bottom left.

1.3.3 Silicon strip tracker

The silicon strip tracker (SST) is the second stage in the CMS tracking system. The top side of Figure 1.15 shows a schematic of the SST. The inner tracker region is composed of the tracker inner barrel (TIB) and the tracker inner disks (TID) covering the region $r < 55$ cm and $|z| < 118$ cm. The TIB is composed of 4 layers while the TID is composed of 3 disks at each end. The silicon sensors in the inner tracker are 320 μm thick, providing a resolution of about 13-38 μm in the $r\phi$ position measurement.

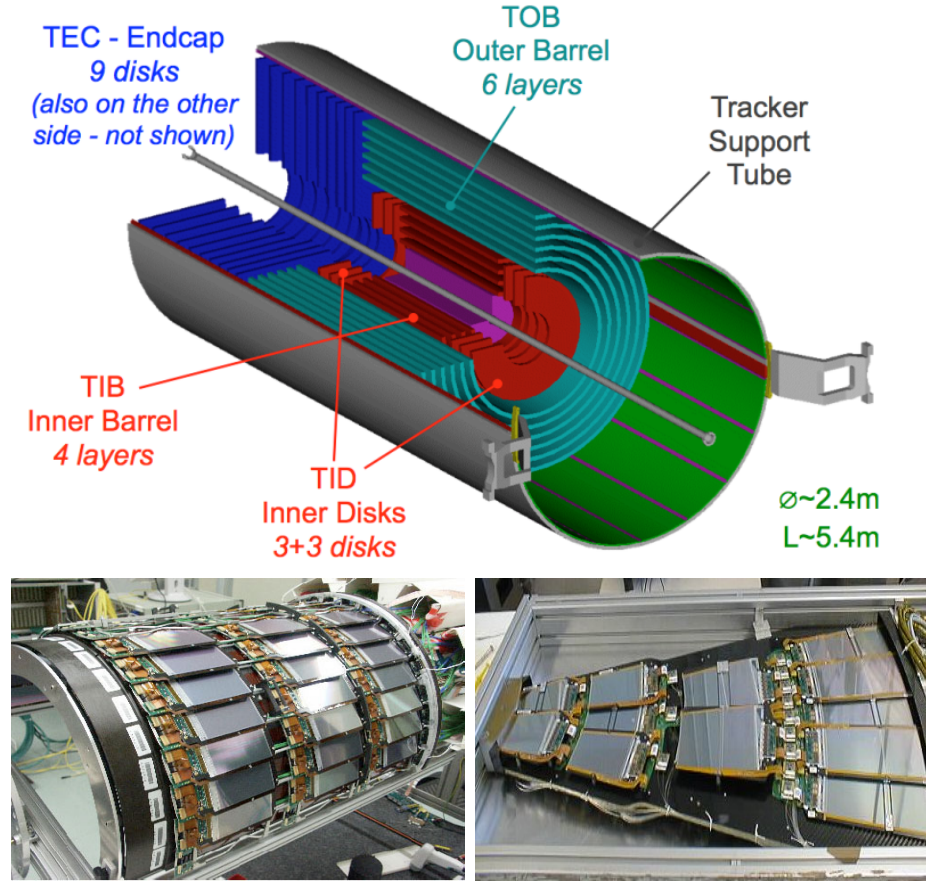


Figure 1.15: Top: CMS Silicon Strip Tracker (SST) schematic view. The SST is composed of the tracker inner barrel (TIB), the tracker inner disks (TID), the tracker outer barrel (TOB) and the tracker endcaps (TEC). Each part is made of silicon strip modules; the modules in blue represent two modules mounted back-to-back and rotated in the plane of the module by a stereo angle of 120 mrad in order to provide a 3-D reconstruction of the hit positions. Bottom: pictures of the TIB (left) and TEC (right) modules [?, ?, ?].

The modules indicated in blue in the schematic view of Figure 1.15 are two modules mounted back-to-back and rotated in the plane of the module by a *stereo* angle of 100 mrad; the hits from these two modules, known as *stereo hits*, are combined to provide a measurement of the second coordinate (z in the barrel and r on the disks) allowing the reconstruction of hit positions in 3-D.

The outer tracker region is composed of the tracker outer barrel (TOB) and the tracker endcaps (TEC). The six layers of the TOB offer coverage in the region $r > 55$

cm and $|z| < 118$ cm, while the 9 disks of the TEC cover the region $124 < |z| < 282$ cm. The resolution offered by the outer tracker is about $13\text{--}38 \mu\text{m}$ in the $r\phi$ position measurement. The inner four TEC disks use silicon sensors $320 \mu\text{m}$ thick; those in the TOB and the outer three TEC disks use silicon sensors of $500 \mu\text{m}$ thickness. The silicon strips run parallel to the z -axis and the distance between strips varies from $80 \mu\text{m}$ in the inner TIB layers to $183 \mu\text{m}$ in the inner TOB layers; in the endcaps the wedge-shaped sensors with radial strips, whose pitch range between $81 \mu\text{m}$ at small radii and $205 \mu\text{m}$ at large radii.

The whole SST has 15148 silicon modules, 9.3 million silicon strips and cover a total active area of about 198 m^2 .

1.3.4 Electromagnetic calorimeter

The CMS electromagnetic calorimeter (ECAL) is designed to measure the energy of electrons and photons. It is composed of 75848 lead tungstate crystals which have a short radiation length (0.89 cm) and fast response, since 80% of the light is emitted within 25 ns; however, they are combined with Avalanche photodiodes (APDs) as photodetectors given that crystals themselves have a low light yield ($30\gamma/\text{MeV}$). A schematic view of the ECAL is shown in Figure 1.16.

Energy is measured when electrons and photons are absorbed by the crystals which generates an electromagnetic *shower*, as seen in bottom right picture of the Figure 1.16; the shower is seen as a *cluster* of energy which depending on the amount of energy deposited can involve several crystals. The ECAL barrel (EB) covers the region $|\eta| < 1.479$, using crystals of depth of 23 cm and $2.2 \times 2.2 \text{ cm}^2$ transverse section; the ECAL endcap (EE) covers the region $1.479 < |\eta| < 3.0$ using crystals of depth 22 cm and transverse section of $2.86 \times 2.86 \text{ cm}^2$; the photodetectors used are

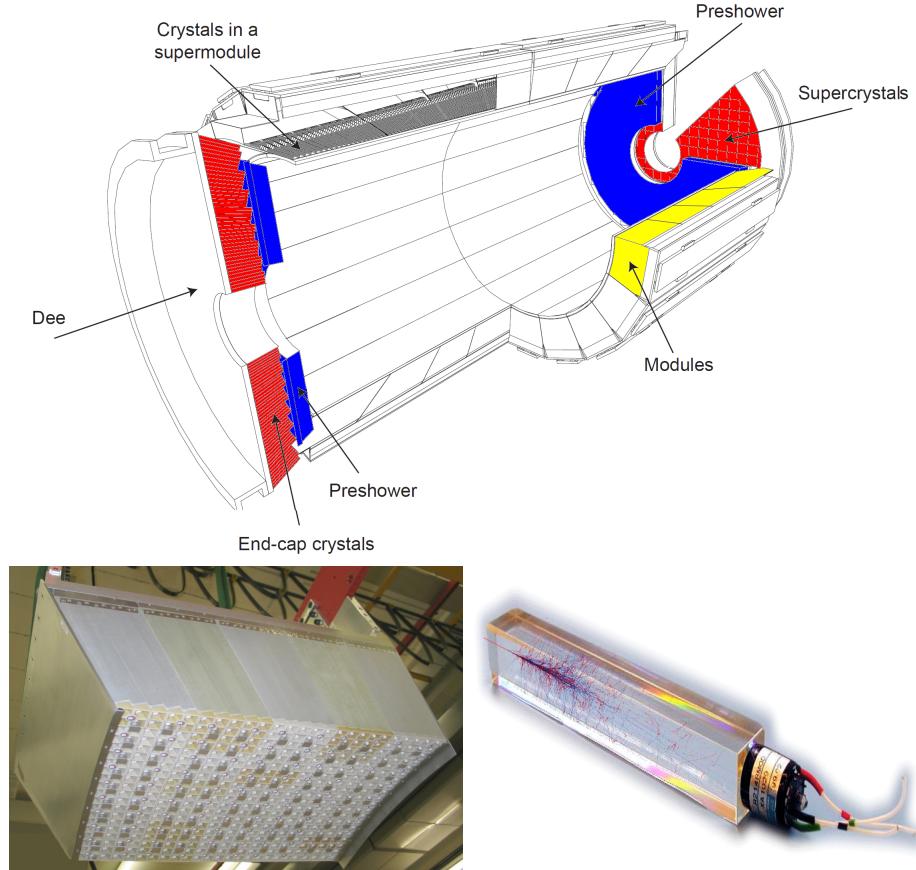


Figure 1.16: Top: CMS ECAL schematic view. Bottom: Module equipped with the crystals (left); ECAL crystal(right) with an artistic representation of an electromagnetic shower [?].

vacuum phototriodes (VPTs). Each EE is divided in two structures called *Dees*.

The preshower detector (ES) is installed in front of the EE and covers the region $1.653 < |\eta| < 2.6$. The ES provides a precise measurement of the position of electromagnetic showers, which allows to distinguish electrons and photon signals from π^0 decay signals. The ES is composed of a layer of lead radiators followed by a layer of silicon strip sensors. The lead radiators initiate electromagnetic showers when reached by photons and electrons, then, the strip sensors measure the deposited energy and the transverse shower profiles. The full ES thickness is 20 cm.

1.3.5 Hadronic calorimeter

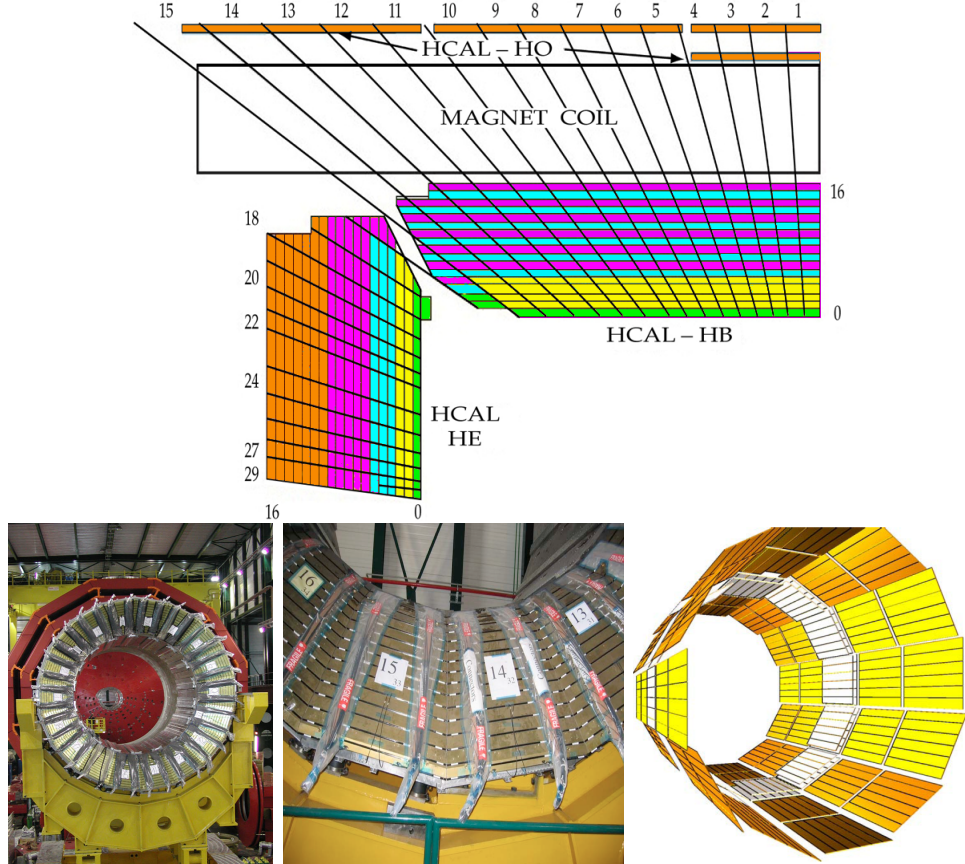


Figure 1.17: Top: CMS HCAL schematic view, the colors indicate the layers that are grouped into the same readout channels. Bottom: picture of a section of the HB; the absorber material is the golden region and scintillators are placed in between the absorber material (left and center). Schematic view of the HO (right). [?, ?]

Hadrons are not absorbed by the ECAL² but by the hadron calorimeter (HCAL), which is made of a combination of alternating brass absorber layers and silicon photomultiplier(SiPM) layers; therefore, particles passing through the scintillator material produce showers, as in the ECAL, as a result of the inelastic scattering of the hadrons with the detector material. Since the particles are not absorbed in the scintillator, their energy is sampled; therefore the total energy is not measured but estimated from

² Most hadrons are not absorbed, but few low-energy ones might be.

the energy clusters, which reduces the resolution of the detector. Brass was chosen as the absorber material due to its short interaction length ($\lambda_I = 16.42$ cm) and its non-magnetivity. Figure 1.17 shows a schematic view of the CMS HCAL.

The HCAL is divided into four sections; the Hadron Barrel (HB), the Hadron Outer (HO), the Hadron Endcap (HE) and the Hadron Forward (HF) sections. The HB covers the region $0 < |\eta| < 1.4$, while the HE covers the region $1.3 < |\eta| < 3.0$. The HF, made of quartz fiber scintillator and steel as absorption material, covers the forward region $3.0 < |\eta| < 5.2$. Both the HB and HF are located inside the solenoid. The HO is placed outside the magnet as an additional layer of scintillators with the purpose of measure the energy tails of particles passing through the HB and the magnet (see Figure 1.17 top and bottom right).

1.3.6 Superconducting solenoid magnet

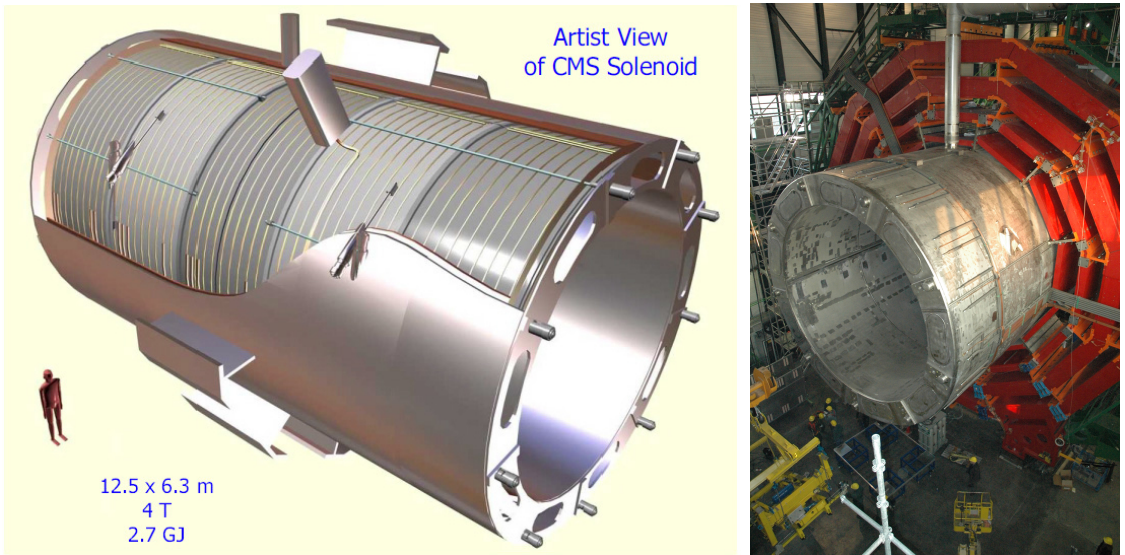


Figure 1.18: Artistic representation of the CMS solenoid magnet(left). The magnet is supported on an iron yoke (right) which also serves as the house of the muon detector and as mechanical support for the whole CMS detector [?].

The superconducting magnet installed in the CMS detector is designed to provide

an intense and highly uniform magnetic field in the central part of the detector. In fact, the tracking system takes advantage of the bending power of the magnetic field to measure with precision the momentum of the particles that traverse it; the unambiguous determination of the sign for high momentum muons was a driving principle during the design of the magnet. The magnet has a diameter of 6.3 m, a length of 12.5 m and a cold mass of 220 ton; the generated magnetic field reaches a strength of 3.8T. Since it is made of Ni-Tb superconducting cable it has to operate at a temperature of 4.7 K by using a helium cryogenic system; the current circulating in the cables reaches 18800 A under normal running conditions. The left side of Figure 1.18 shows an artistic view of the CMS magnet, while the right side shows a transverse view of the cold mass where the winding structure is visible.

The yoke (see Figure 1.18), composed of 5 barrel wheels and 6 endcap disks made of iron, serves not only as the media for magnetic flux return but also provides housing for the muon detector system and structural stability to the full detector.

1.3.7 Muon system

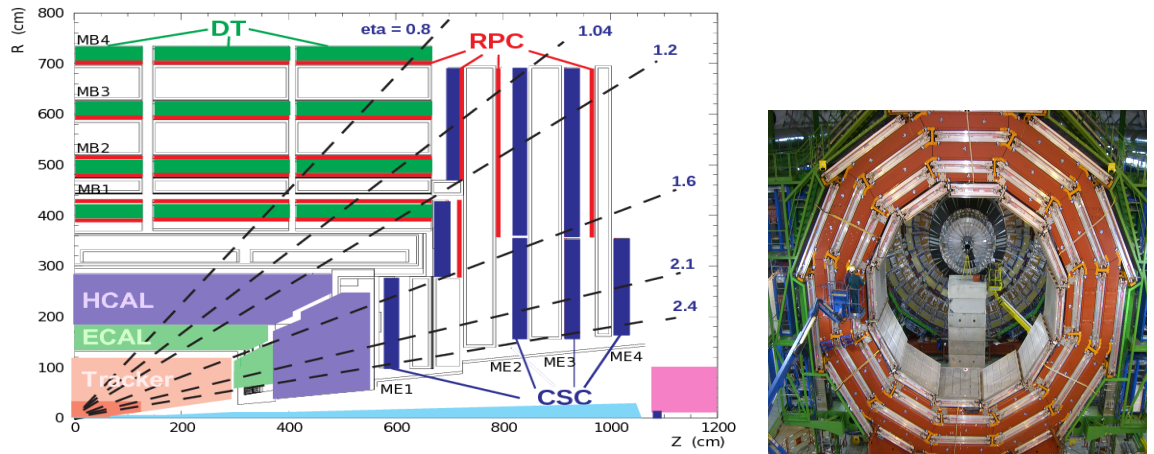


Figure 1.19: Left: CMS muon system schematic view; Right: one of the yoke rings with the muon DTs and RPCs installed; in the back it is possible to see the muon endcap [?].

Muons are the only charged particles able to pass through all the CMS detector due to their low ionization energy loss; thus, muons can be separated easily from the high amount of particles produced in a pp collision. Also, muons are expected to be produced in the decay of several new particles; therefore, good detection of muons was one of the leading principles when designing the CMS detector.

The CMS muon detection system (muon spectrometer) is embedded in the return yoke as seen in Figure 1.19. It is composed of three different detector types, the drift tube chambers (DT), cathode strip chambers (CSC), and resistive plate chambers (RPC); DT are located in the central region $\eta < 1.2$ arranged in four layers of drift chambers filled with an Ar/CO₂ gas mixture.

The muon endcaps are made of CSCs covering the region $\eta < 2.4$ and filled with a mixture of Ar/CO₂/CF₄. The reason behind using a different detector type lies on the different conditions in the forward region like the higher muon rate and higher residual magnetic field compared to the central region.

The third type of detector used in the muon system is a set of four disks of RPCs working in avalanche mode. The RPCs provide good spatial and time resolutions. The track of high- p_T muon candidates is built combining information from the tracking system and the signal from up to six RPCs and four DT chambers.

The muon tracks are reconstructed from the hits in the several layers of the muon system.

1.3.8 CMS trigger system

CMS expects pp collisions every 25 ns, i.e., an interaction rate of 40 MHz for which it is not possible to store the recorded data in full. In order to handle this high event rate data, an online event selection, known as triggering, is performed; triggering

reduces the event rate to 100 Hz for storage and further offline analysis.

The trigger system starts with a reduction of the event rate to 100 kHz in the so-called *the level 1 trigger* (L1). L1 is based on dedicated programmable hardware like Field Programmable Gate Arrays (FPGAs) and Application Specific Integrated Circuits (ASICs), partly located in the detector itself; another portion is located in the CMS underground cavern. Hit pattern information from the muon chambers and the energy deposits in the calorimeter are used to decide if an event is accepted or rejected, according to selection requirements previously defined, which reflect the interesting physics processes. Figure 1.20 shows the L1 trigger architecture.

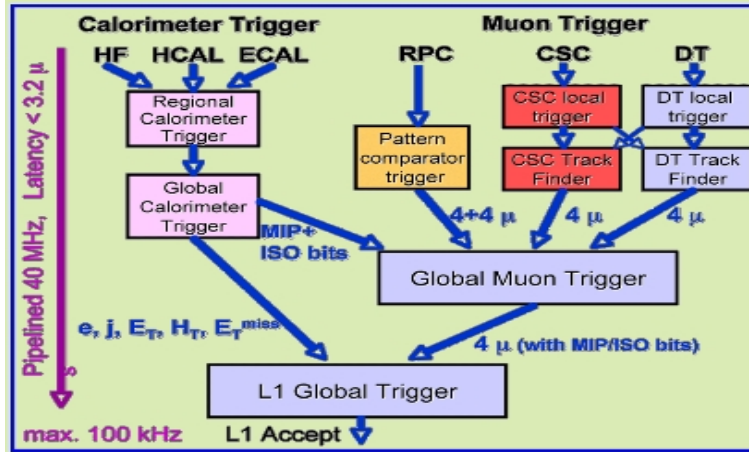


Figure 1.20: CMS Level-1 trigger architecture [?].

The second stage in the trigger system is called *the high-level trigger* (HLT); events accepted by L1 are passed to HLT in order to make an initial reconstruction of them. HLT is software based and runs on a dedicated server farm, using selection algorithms and high-level object definitions; the event rate at HLT is reduced to 100 Hz. The first HLT stage takes information from the muon detectors and the calorimeters to make the initial object reconstruction; in the next HLT stage, information from the pixel and strip detectors is used to do first fast tracking and then full tracking online. This initial object reconstruction is used in further steps of the trigger system.

Events and preliminary reconstructed physics objects from HLT are sent to be fully reconstructed at the CERN computing center known also as Tier-0 facility. Again, the pixel detector information provides high-quality seeds for the track reconstruction algorithm offline, primary vertex reconstruction, electron and photon identification, muon reconstruction, τ identification, and b-tagging. After full reconstruction, data sets are made available for offline analyses.

Sometimes, a trigger *prescale* is introduced in order to reduce even further the event rate; thus, for a prescaling of ten only one of each ten events passing the trigger requirements is saved.

References

- [1] Matthias U. Mozer. Electroweak Physics at the LHC. *Springer Tracts Mod. Phys.*, 267:1–115, 2016.
- [2] Gennadi Sardanashvily. *Noether’s theorems: applications in mechanics and field theory*. Atlantis studies in variational geometry. Springer, Paris, 2016.
- [3] Steven Weinberg. The Making of the Standard Model. *Eur. Phys. J. C*, 34(hep-ph/0401010):5–13. 21 p. ; streaming video, 2003.
- [4] Roger Wolf. *The Higgs Boson Discovery at the Large Hadron Collider*, volume 264. Springer, 2015.
- [5] Jose Andres Monroy Montanez, Kenneth Bloom, and Aaron Dominguez. Search for production of a Higgs boson and a single Top quark in multilepton final states in pp collisions at $\sqrt{s} = 13$ TeV, Jul 2018. Presented 23 Jul 2018.
- [6] Peisi Huang, Aniket Joglekar, Min Li, and Carlos E. M. Wagner. Corrections to di-Higgs boson production with light stops and modified Higgs couplings. *Phys. Rev.*, D97(7):075001, 2018.
- [7] Matthew J. Dolan, Christoph Englert, and Michael Spannowsky. New Physics in LHC Higgs boson pair production. *Phys. Rev.*, D87(5):055002, 2013.

- [8] Shinya Kanemura, Kunio Kaneta, Naoki Machida, Shinya Odori, and Tetsuo Shindou. Single and double production of the Higgs boson at hadron and lepton colliders in minimal composite Higgs models. *Phys. Rev.*, D94(1):015028, 2016.
- [9] Albert M Sirunyan et al. Search for Higgs boson pair production in the $\gamma\gamma b\bar{b}$ final state in pp collisions at $\sqrt{s} = 13$ TeV. 2018.
- [10] Alexandra Oliveira. Gravity particles from Warped Extra Dimensions, predictions for LHC. 2014.
- [11] Lisa Randall and Raman Sundrum. A Large mass hierarchy from a small extra dimension. *Phys. Rev. Lett.*, 83:3370–3373, 1999.
- [12] Kunihiro Uzawa, Yoshiyuki Morisawa, and Shinji Mukohyama. Excitation of Kaluza-Klein gravitational mode. *Phys. Rev.*, D62:064011, 2000.
- [13] H. Davoudiasl, J. L. Hewett, and T. G. Rizzo. Phenomenology of the Randall-Sundrum Gauge Hierarchy Model. *Phys. Rev. Lett.*, 84:2080, 2000.
- [14] Michael Forger and Hartmann Romer. Currents and the energy momentum tensor in classical field theory: A Fresh look at an old problem. *Annals Phys.*, 309:306–389, 2004.
- [15] Chuan-Ren Chen and Ian Low. Double take on new physics in double Higgs boson production. *Phys. Rev.*, D90(1):013018, 2014.
- [16] Roberto Contino, Margherita Ghezzi, Mauro Moretti, Giuliano Panico, Fulvio Piccinini, and Andrea Wulzer. Anomalous Couplings in Double Higgs Production. *JHEP*, 08:154, 2012.

- [17] Richard Phillips Feynman, Robert Benjamin Leighton, and Matthew Sands. *The Feynman lectures on physics; New millennium ed.* Basic Books, New York, NY, 2010. Originally published 1963-1965.
- [18] Savas Dimopoulos, Stuart Raby, and Frank Wilczek. Proton decay in supersymmetric models. *Physics Letters B*, 112(2):133 – 136, 1982.
- [19] David J Griffiths. *Introduction to elementary particles; 2nd rev. version.* Physics textbook. Wiley, New York, NY, 2008.
- [20] M. Della Negra, P. Jenni, and T. S. Virdee. Journey in the search for the higgs boson: The atlas and cms experiments at the large hadron collider. *Science*, 338(6114):1560–1568, 2012.
- [21] Jennifer Ouellette. Einstein’s quest for a unified theory. *APS*, 2015.
- [22] E A Davis and Isabel Falconer. *J.J. Thompson and the discovery of the electron.* Taylor and Francis, Hoboken, NJ, 2002.
- [23] Oreste Piccioni. *The Discovery of the Muon*, pages 143–162. Springer US, Boston, MA, 1996.
- [24] G. Danby, J-M. Gaillard, K. Goulian, L. M. Lederman, N. Mistry, M. Schwartz, and J. Steinberger. Observation of high-energy neutrino reactions and the existence of two kinds of neutrinos. *Phys. Rev. Lett.*, 9:36–44, Jul 1962.
- [25] M. L. Perl, G. S. Abrams, and et al Boyarski. Evidence for anomalous lepton production in $e^+ - e^-$ annihilation. *Phys. Rev. Lett.*, 35:1489–1492, Dec 1975.
- [26] K. Kodama et al. Observation of tau neutrino interactions. *Phys. Lett.*, B504:218–224, 2001.

- [27] S. M. Bilenky. Neutrino in Standard Model and beyond. *Phys. Part. Nucl.*, 46(4):475–496, 2015.
- [28] S Chandrasekhar. *Newton's principia for the common reader*. Oxford Univ., Oxford, 2003. The book can be consulted by contacting: PH-AID: Wallet, Lionel.
- [29] Hanoch Gutfreund and Jürgen Renn. *The road to relativity: the history and meaning of Einstein's "The foundation of general relativity" : featuring the original manuscript of Einstein's masterpiece*. Princeton University Press, Princeton, NJ, Apr 2015.
- [30] J. Butterworth. *Smashing Physics*. Headline Publishing Group, 2014.
- [31] W N Cottingham and D A Greenwood. *An Introduction to the Standard Model of Particle Physics; 2nd ed.* Cambridge Univ. Press, Cambridge, 2007.
- [32] Eric W. Weisstein. Fundamental forces.
- [33] Carl Bender. Mathematical physics.
- [34] Andrew Wayne. QED and the Men Who Made It: Dyson, Feynman, Schwinger, and Tomonaga by Silvan S. Schweber. *The British Journal for the Philosophy of Science*, 46(4):624–627, 1995.
- [35] C. Patrignani et al. Review of Particle Physics. *Chin. Phys.*, C40(10):100001, 2016.
- [36] Michelangelo L Mangano. Introduction to QCD. (CERN-OPEN-2000-255), 1999.
- [37] Matt Strassler. Of particular significance: Conversations about science with theoretical physicist matt strassler.

- [38] S. L. Glashow. Partial Symmetries of Weak Interactions. *Nucl. Phys.*, 22:579–588, 1961.
- [39] F. Englert and R. Brout. Broken symmetry and the mass of gauge vector mesons. *Phys. Rev. Lett.*, 13:321–323, Aug 1964.
- [40] Peter W. Higgs. Broken symmetries and the masses of gauge bosons. *Phys. Rev. Lett.*, 13:508–509, Oct 1964.
- [41] G. S. Guralnik, C. R. Hagen, and T. W. B. Kibble. Global conservation laws and massless particles. *Phys. Rev. Lett.*, 13:585–587, Nov 1964.
- [42] Pauline Gagnon. *Who cares about particle physics? : making sense of the Higgs boson, the Large Hadron Collider and CERN*. Oxford University Press, 2016.